Structural analysis and tracking of micron-sized glass particles during shear deformation: A study based on time-resolved tomographic data

L. Handl[a,*], L. Torbahn[b], A. Spettl[a], V. Schmidt[a], A. Kwade[b]

[a] *Insitute of Stochastics, Universität Ulm, Helmholtzstr. 18, 89069 Ulm, Germany*
[b] *Institute for Particle Technology (iPAT), Technische Universität Braunschweig, Volkmaroder Str. 5, 38104 Braunschweig, Germany*

Abstract

The interplay between structure and mechanical properties of fine and cohesive granular matter is of wide interest and far from being well understood. In order to study this relationship experimentally, it is desirable to record as much information on the particles and their motion behavior as possible during a shear experiment — ideally, the trajectory of every single particle. Observing the particle movements offers deep insights into changes in the mechanical behavior of the bulk (e.g., densification, loosening or formation of failure areas) and into the behavior of single particles. However, obtaining particle-level information on the dynamics of an entire shear-tester experiment remains a great challenge. In this paper we present an experiment and analysis methods which allow the extraction of the trajectories of almost all particles within a shear-tester. A fully functional micro shear-tester was developed and implemented into an X-ray microtomography device. With this combination we can visualize all particles within small bulk volumes of the order of a few µl under well-defined mechanical manipulation. The processing of time-resolved tomographic data makes it possible to localize and track particles despite large angle increments of up to 5° between tomographic measurements. We apply our methods to a torsional shear experiment with spherical micron-sized particles (~ 30 µm) and analyze the structural evolution of the sample. In addition, particle tracks provide detailed insights into the formation and evolution of the shear band.

Keywords: shear flow, glass beads, micro shear-tester, particle tracking, X-ray microtomography

1. Introduction

Shear flow of granular media is ubiquitous in nature and of industrial importance when it comes to the handling and processing of bulk solids (e.g., flow through hoppers [1, 2], bunkers and silos [3, 4]). In the physics of granular matter [5], among many other interesting phenomena, understanding the flow properties, i.e., the stress response to an applied strain rate, has been in the focus of research [6]. At slow, quasi-static deformation, there arises a strain rate independent creep regime [7, 8]. The localization of strain within the bulk, often referred to as failure zone or shear band, represents a unique feature of this quasi-static regime, which was addressed by many researchers in the past [9, 10, 11, 12] and can be observed, e.g., in glassy systems [13] and solidifying metals [14] as well. However, the interplay of structure and mechanical properties of the bulk solid is still not deciphered sufficiently, especially when it comes to cohesive granular matter.

Experimental investigations of this interplay are challenging because they require detailed information on particle properties, packing structure and dynamics over the course of a shear experiment — ideally, down to single-particle trajectories. Sophisticated experimental setups are capable of determining the properties of individual micron-sized particles [15] and of imaging the inner structure of a bulk solid nondestructively, e.g., via computer tomography [16, 17]. However, detailed experimental information on the dynamics of small-size particles and on their trajectories in 3D is still particularly rare.

An alternative route of investigation is offered by numerical simulations with the discrete element method (DEM), which provide valuable insight into the mechanical behavior of granular matter [18, 19, 20]. Although DEM simulations output fine-grained information on particle trajectories and even forces acting between them, the accuracy of the physical behavior in the models is limited by computational constraints and the high complexity in contact mechanics of micron-sized particles [21]. Consequently, even when following the DEM approach, experimental data on the trajectories of micron-sized particles under shear is highly needed for model validation.

The main challenge of tracking all particles within a bulk volume is that it requires 3D image data in a sufficiently high spatial and temporal resolution. Standard methods, which rely on one or more 2D cameras to analyze the dynamics in a flow, provide only aggregated information or are restricted to transparent liquids containing a relatively small number of tracer particles (e.g., particle image velocimetry [22, 23, 24] or particle tracking velocimetry [25, 26]). Moreover, to our knowledge, these techniques have not yet been applied to micron-sized particles. An alternative approach is presented in [27], where confocal laser microscopy is used to obtain 3D images of particles under lateral shear. While this imaging technique allows for a high temporal resolution, it limits the size of the sample in z-

*Corresponding author. Tel: +49 731/50-23528; Fax: +49 731/50-23649
Email address: lisa.handl@uni-ulm.de (L. Handl)

direction and requires particles to be surrounded by a fluid with matching refractive index. This is not possible for all particle materials or when investigating dry powders. Interestingly, partial photobleaching of individual particles enables the detection of particle rotations.

In this paper we use a fully functional micro-sized shear-tester [16], which can be fitted into an X-ray microtomography (XMT) device. In contrast to [16], we conduct and analyze a torsional shear experiment with constant normal load and analyze the motion of almost all micron-sized spherical particles on particle level. Using the XMT, a series of 3D images is recorded in the course of the experiment. While the XMT provides high-quality 3D images at very high spatial resolution, each measurement is time consuming. Therefore, only a limited temporal resolution can be realized. To overcome the problem of tracking particles despite the low temporal resolution, we propose a method to estimate the average particle movement at any location in the shear cell directly from the image data, building on ideas from [28]. Our approach is data-driven and explores the rotational symmetry of the shear cell. Based on this first estimate, we are able to extract the trajectories of almost all individual particles in the shear cell. We utilize this data to examine the initial shear band formation and its evolution over time in full detail. In addition, we analyze structural inhomogeneities in the sample over time.

Our dataset is extraordinary in that it provides experimental particle-level information on the dynamics within the entire shear cell. Thus, our methods allow to fully analyze and compare experiments both on particle level and macroscopically. Similar information is usually only obtained by DEM simulations. Therefore, our methods offer an increased validation depth for DEM simulations and a reliable basis for model calibration, although a direct comparison of our experiment to DEM simulations exceeds the scope of this paper. In contrast to [27], our methods are applicable to dry powders and to almost all particle materials. Finally, the micro shear-tester is also well suited for determining shear flow properties of powders which are only available in small quantities, e.g. for screening processes.

The paper is structured as follows. Sections 2.1 and 2.2 are devoted to the model material and experimental setup. The methodology of image segmentation, image-based measurement of local shear deformation and particle tracking is described in Section 2.3. Results of a detailed analysis of structural inhomogeneity as well as shear band formation and evolution are presented in Section 3 and discussed in Section 4.

2. Material and methods

2.1. Material

In this study we use a fine and slightly cohesive powder which consists of solid borosilicate glass microspheres (BSGMS 27-32 µm, CoSpheric LLC, USA; BSGMS in the following). An image of several microsphere particles taken on a scanning electron microscope (SEM) is presented in Figure 1 (inset). The figure emphasizes the almost uniform spherical

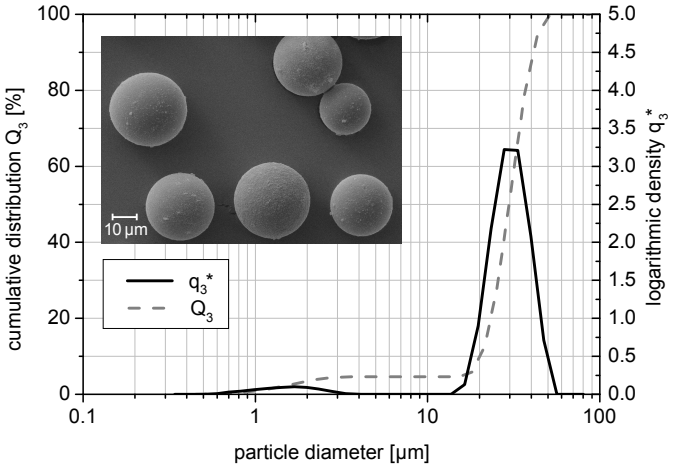

Figure 1: Particle size distribution (mass distribution, logarithmic density and cumulative distribution function) and SEM picture (inset) of BSGMS glass particles.

shape and similar size of the particles, but also shows a non-negligible surface roughness. We measured the particle size distribution using laser diffraction (Helos, Sympatec GmbH, Germany) after dispersing the particles with ultrasound for 30 s in an aqueous environment. The results, which are shown in Figure 1, indicate a narrow mono-disperse size distribution of the glass particles with median value $x_{50,3} \approx 30$ µm.

Particle stiffness and adhesion forces were determined in [28] using nanoindentation and atomic force microscopy (AFM), respectively. Nanoindentation was carried out with the Triboindenter (Hysitron, Inc, USA), placing single particles between a glass object slide and a flat punch. They were deformed using a force-controlled approach with a maximum loading force of 2 mN. Then, Young's modulus has been calculated from the resulting stress-strain curve taking Hertz theory as a basis. The AFM measurements have been realized by the XE 100 (Park Systems, Korea) using the colloidal probe method for pairs of particles. One of the two particles was attached to the apex of a tip-less cantilever with UV-hardened glue. The other one was attached to the object slide with nail varnish. Then, both particles were brought into contact and the force needed to break this contact was determined. Since both measurement techniques are subject to strong fluctuations, nanoindentation has been repeated for 58 particles and AFM has been applied to 100 pairs of particles. The mean values and standard deviations reported in [28] are $E = 15 \pm 7$ GPa for the elastic modulus and $F_c = 82$ nN $\pm$ 60 nN for adhesion forces. From a methodological point of view we do not expect a major influence of the variability on our results.

2.2. Experiment

2.2.1. X-ray microtomography (XMT)

The fundamental component for a detailed microstructural investigation is the nondestructive examination with the XMT, which enables an image-based analysis. We use a high-resolution tomography device (MicroXCT-400, Zeiss (Xradia), Germany). For this study an acceleration voltage of 50 kV and

a current intensity of 200 µA were applied at the X-ray source. These parameters result in the best outcome for high-contrast images. According to the sample diameter of 2 mm, a ten-fold optical magnification is used to ensure a reproduction of the entire sample diameter with a resolution of 2.2 µm (1.1 µm before binning). A single detector collected the X-rays which were emitted from the source and passed through the sample, resulting in an intensity grayscale image. In order to get an accurate 3D reconstruction afterwards, we measured 2000 of these projections for various angles of rotation around the central axis of the sample. The reconstructed data is stored in stacks of 2D images for later analysis with regard to structure and dynamics. Depending on the device resolution and the particle size, investigations on mesoscale as well as on particle scale are possible. Thus, the detailed data on particle scale qualifies for finding relations between particle parameters (e.g., size, shape and aspect ratio) and mesoscale or bulk behavior (e.g., shear zone characteristics).

2.2.2. Micro shear-tester

The torsional micro shear-tester with cylindrical shear cell geometry was developed to handle very small sample volumes in the range of 6-15 µl [28]. In combination with the XMT, the samples can easily be manipulated in terms of compression and shear deformation on the one hand, and imaged in 3D at a very high resolution on the other hand. A cylindrical sample chamber with a radius of $R = 1$ mm allows for an (in principle) infinite torsional shear movement. The sample chamber is a very fine borosilicate glass capillary with a side wall thickness of 50 µm and is confined by an upper and lower piston in vertical direction. The pistons can be flat for simple compression tests or structured with six vanes arranged in a regular star shape for shear tests like presented in this work. A schematic image of the shear cell can be found in Figure 2. During shear, the upper piston and outer wall move whereas the lower piston measures the normal force and torque. For this purpose, a magnetic spring was included at the lower piston as well as a frictionless air suspension to prevent or at least minimize friction. A major advantage of this system is the decoupled determination of force and torque. Loads in the range of 0.1-20 kPa can be applied by the micro shear-tester.

The sample is prepared by sieving the particles into the glass capillary in order to avoid agglomeration. The normal load is increased up to $\sigma = 0.5$ kPa and kept constant in the following shear process. During shear, the upper piston and wall are rotated in steps of 0.5° up to 9.5°. After 9.5° the angle increment is increased to 5° until an entire rotation of 39.5° is achieved. The experiment is carried out quasi-statically with an angular velocity of $\omega = 0.1$ °/s. Directly after densification and after each step of shearing an XMT measurement of the entire shear cell is recorded. The resulting 3D image stacks are aligned and cut to the size of the sample chamber, so that they have the same dimension in x- and y-direction but different sizes in z-direction (depending on dilation/densification during shear). The maximum z-coordinate of the image stack recorded at time t is denoted by $z^t_{\max}$, where t is the time of shearing — i.e., we neglect the pauses necessary for XMT measurements.

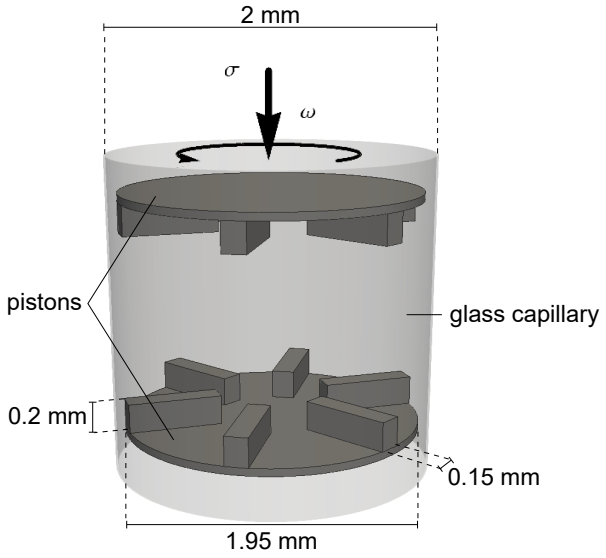

Figure 2: Schematic view of the shear cell of the micro shear-tester.

2.3. Analysis

2.3.1. Image-based local shear deformation

A first approximation of the local shear deformation is computed directly from the image data in a similar way as proposed in [28]. The idea of this approach is to compare the image slices at two successive points in time and a fixed height z. The local shear angle at height z is the angle by which the first slice has to be rotated so that it best matches the second slice. This approach relies on a strong similarity between the particle structures at two consecutive points in time. Thus, it requires a sufficiently high spatial and temporal resolution.

The quality criterion used in this study to determine how closely the two slices match is the image cross-correlation,

$$\mathrm{corr}(I, J) = \frac{\sum_{x,y}(I(x,y) - \bar{I})(J(x,y) - \bar{J})}{\sigma_I \cdot \sigma_J}, \qquad (1)$$

where $I = \{I(x,y)\}$ and $J = \{J(x,y)\}$ are digital 2D images, $\bar{I}$ and $\bar{J}$ are the mean values, and σ_I and σ_J are the standard deviations of gray values taken over all pixels in I and J, respectively. For a time step (t_1, t_2) the local angle of shear deformation at height z is estimated by computing

$$\Delta_\varphi^{t_1 \to t_2}(z) = \underset{\alpha \in [-1°,\ \Delta\varphi_s(t_1,t_2)+1°]}{\arg\max} \left\{ \mathrm{corr}\left(\mathrm{rot}_\alpha(I^z_{t_1}), I^z_{t_2} \right) \right\}, \qquad (2)$$

where I^z_t denotes the slice at height z and time t, rot_α denotes the rotation around the image center by the angle α, and $\Delta\varphi_s(t_1, t_2)$ is the angle increment used in time step (t_1, t_2). Theoretically, optimization over the full range $\alpha \in [0, 360]$ would be desirable. For computational reasons we restrict it to a realistic range in Equation (2). The image rotations are carried out using bilinear interpolation and the maximization is implemented in discrete steps of 0.1°. Applying the same procedure for all available z-coordinates yields a spatially resolved local shear deformation over the full height of the sample.

The same methodology can be used to measure the rotation of the upper and lower piston in the image data. This is necessary because there may be differences between the targeted and actual movements of the pistons, which will be discussed in more detail later (cf. Section 3.2). We simply average $\Delta_\varphi^{t_1\to t_2}(z)$ over the range of z-coordinates in which the upper and lower piston, respectively, are visible. Since an exact measurement of these movements is crucial for a correct normalization of particle velocities later on (and less computationally expensive than estimating $\Delta_\varphi^{t_1\to t_2}(z)$ over the full height of the sample), optimization is carried out in steps of 0.01°.

The idea of estimating shear deformation locally from the image data can be extended further to capture radial variations of the local deformation and to estimate local compression or dilation along with the rotational deformation. For this purpose, each image slice is subdivided into k disjoint and concentric rings of equal area, $R_1, \ldots, R_k$, and a rotational *and* translational deformation are applied simultaneously. This means that instead of rotating the image slice as a whole, each ring is rotated independently and shifted vertically so that it best matches the corresponding region of the next image stack. We then obtain the 2D maximization problem

$$\left(\Delta_\varphi^{t_1\to t_2}(z, r_i),\ \Delta_z^{t_1\to t_2}(z, r_i)\right) = \underset{\substack{h\in[h_{\min},\ldots,h_{\max}]\\ \alpha\in[-1°,\ \Delta\varphi_s(t_1,t_2)+1°]}}{\arg\max} \left\{\operatorname{corr}\left(\operatorname{rot}_\alpha(I_{t_1}^{z,R_i}), I_{t_2}^{z+h,R_i}\right)\right\}, \tag{3}$$

where r_i is the central radius of R_i, I_t^{z,R_i} denotes the ring R_i of the image slice at height z and time t, and $i \in \{1, \ldots, k\}$. The result is a local angle of shear and a local vertical deformation for each z-coordinate and ring, R_i. Using bilinear interpolation we can calculate values for the deformation at arbitrary locations in the sample. In this study $k = 10$ rings are used and the range for the vertical shift is chosen based on the stack sizes in z-direction, $z_{\max}^{t_1}$ and $z_{\max}^{t_2}$, as

$$[h_{\min}, \ldots, h_{\max}] = \left[\min\{z_{\max}^{t_2} - z_{\max}^{t_1}, 0\}, \ldots, \max\{z_{\max}^{t_2} - z_{\max}^{t_1}, 0\}\right].$$

In the following, we will refer to the left-hand sides of Equations (2) and (3) as 1D and 2D image-based local shear deformation, respectively. Both methods are applied and discussed in this paper.

2.3.2. *Image segmentation*

In order to extract information on single particles from the image data, 3D images are segmented using a marker-based watershed transformation [29]. First, the grayscale images are smoothed using a Gaussian filter with a small standard deviation of 1 voxel side length, and binarized using the IsoData algorithm implemented in ImageJ [30]. Subsequently, small disconnected pores are filled with solid. This step is needed because a small percentage of the particles is hollow. The negative of the Euclidean distance transform (distances from particle voxels to the pore phase) forms the relief on which the watershed transformation is run.

A common choice for the markers is to select the local maxima of the Euclidean distance transform [29]. However, this choice tends to promote over-segmentation since minor surface roughnesses can lead to multiple local maxima within one particle. In the present study this problem is avoided by using an approach presented in [27], where the original grayscale images are convolved with a mask resembling the appearance of a particle. After convolution, the particle centers appear as smooth and isolated local intensity maxima. These maxima are extracted from the convolved images and used as markers for the watershed transformation. The convolution technique is ideal for spherical particles with a narrow size distribution as used in this study, although it can be adapted for broader size distributions as shown in [27]. The main steps of the segmentation process are visualized in Figure 3.

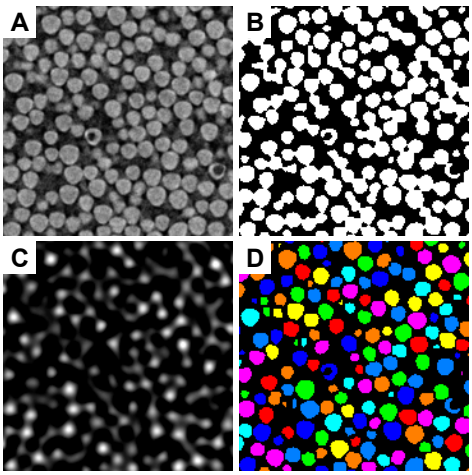

Figure 3: Visualization of the main steps of the segmentation process based on a small cutout of an image slice. Grayscale image obtained by XMT (A), binary image (B), convolution of grayscale image and particle mask used for marker selection (C) and final segmentation result after applying the marker-based watershed transform (D). Note that though the visualization is in 2D, all operations are carried out in 3D.

2.3.3. *Particle tracking*

Based on the centroids of the particles in the segmented binary images, a particle tracking is performed. The tracking algorithm used in this study for time steps with an angle increment of 0.5° has been proposed in [31] and aims to minimize the sum of squared displacements in each time step. For computational reasons the optimization is not carried out directly in [31], but on a reduced problem. Assignments between particles of two consecutive points in time are discarded if the distance between the particles exceeds a certain threshold, s. This simplification typically leads to a decomposition of the optimization problem into a number of smaller problems, which can be solved independently and much faster. The threshold value has been set to $s = 19.8$ µm in the current study.

Minimizing the sum of squared displacements is feasible as long as very little movement occurs within a time step. In particular, particle movements in one step have to be less than the threshold value, s. This is most likely true for shearing steps of 0.5° since a particle will be displaced by at most 8.72 µm theoretically (arc length at the upper, outer edge of the cylinder). However, when shearing in steps of 5°, particle displacements

of ten times the size, i.e., of up to 87.2 µm, have to be expected. In this case a tracking computed by minimizing displacements will clearly be wrong and it is impossible to obtain satisfying results without prior information on the dynamics in the particle system.

The 2D image-based local shear deformation (cf. Section 2.3.1) essentially describes the average movement of particles depending on their location in the sample — and this is used as prior information for tracking particles in steps with an angle increment of 5°. For every particle at time t_1, a hypothetical position for where it is expected to be at time t_2 is calculated based on the 2D image-based local shear deformation, $(\Delta_\varphi^{t_1\to t_2}, \Delta_z^{t_1\to t_2})$. This is done by rotating each particle center (r_p, φ_p, z_p) around the central axis of the cylinder by the angle $\Delta_\varphi^{t_1\to t_2}(z_p, r_p)$ and shifting it vertically by $\Delta_z^{t_1\to t_2}(z_p, r_p)$. Then, the sum of squared distances between the hypothetical and actual particle positions at time t_2 is minimized, where now all assignments leading to a larger distance between hypothetical and actual position than some threshold, $\tilde{s}$, are discarded. Here we obtained good results for $\tilde{s} = 17.6$ µm.

This approach for tracking in steps of 1° or more is validated using the data from 3.5° to 9.5° of shearing, which is available in steps of 0.5° and where no more major compression occurs. For this whole period, a particle tracking has been computed based on all available data and the original method described in [31]. This will be referred to as reference tracking in the following. In order to validate the tracking method based on the local shear deformation, it has been applied to each of the intervals from 3.5° to 4°, from 3.5° to 4.5°, ..., and from 3.5° to 9.5° of shearing, taking into account only the first and last point in time, respectively. In particular, no information on intermediate time steps is used. The resulting tracks have been compared to the ground truth, i.e., each track is considered correct if its starting and end point belong to the same track in the reference tracking. The fraction of correct tracks decreases slowly with increasing angle increment. For an angle increment of 5° (or smaller) more than 98.5 % of the computed tracks agree with the reference tracking. Even with an angle increment of 6°, more than 98 % of the tracks are correct.

2.3.4. Estimating the axis of rotation

When analyzing the tracked particle data it becomes apparent that the empirical axis of rotation does not necessarily coincide with the central axis of the cylindrical sample (see Figure 4). The deviations can be caused by small inaccuracies in the alignment of the glass capillary and the upper and lower piston in the experiment, cf. Section 2.2.2, and lead to an overestimation of angular velocities on the one side and to an underestimation on the other side of the cylinder. In order to adjust for these effects, the axis of rotation is estimated from the data.

If rotation around a roughly vertical axis occurs, particles with the same height and horizontal distance from the axis of rotation will have approximately the same velocity. This means that the center of rotation at a given height can be estimated by fitting a circle to the particles at this height which have similar velocities. Note that the velocity of a particle is measured as the distance it travels per degree of shearing, i.e., it has the unit µm/°. For a grid of heights and velocities the corresponding particles are collected and a circle parallel to the xy-plane is fitted to their centers using weighted least squares, where the weight of each particle is determined by how closely it matches the velocity and z-coordinate of interest. More precisely, the weight of a particle p in the circle fitting for height z and velocity v is given by

$$w_p(z, v) = \exp\left(-\frac{(z - z_p)^2}{2h_z^2} - \frac{(v - v_p)^2}{2h_v^2}\right), \tag{4}$$

where z_p and v_p are the z-coordinate and velocity of p, and h_z and h_v are smoothing parameters. The center of rotation at height z is then determined by calculating the average of the circle centers fitted for height z, i.e., over all velocities in the grid. Note that the axis of rotation estimated in this way does not necessarily need to be a straight line but can be curved. In addition, the (curved) axis depends on the time step for which velocities have been computed, so it can change over time.

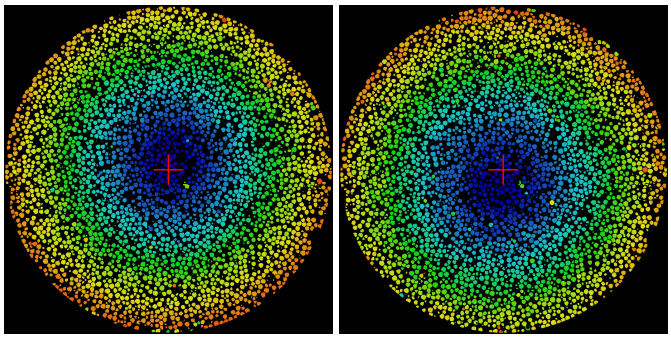

Figure 4: Slice of the binary image at two different points in time. Each particle is colored according to the distance it travels in the subsequent time step, blue indicates small and red indicates large values. In the first time step (left) the center of rotation is slightly above and in the second time step (right) it is below and left of the center of the sample. The image centers are marked with a red cross.

The smoothing parameters h_z and h_v control how many particles are relevant for each circle fitting. They should be large enough so that the circle fitting yields stable results, and small enough to allow the estimated circle centers to vary with height and velocity. In the present study they have been set to $h_z = 11$ µm and $h_v = 0.66$ µm/°. For these parameters, the resulting axis is a smooth but flexible 3D curve.

Note that no rotation occurs at the bottom of the sample. Here, all particles have a velocity close to zero and therefore approximately the same weight in the circle fitting. Due to the cylindrical shape of the domain, the estimated axis of rotation will automatically be dragged towards the center of the sample in these regions.

3. Results

In order to analyze the shear induced structural heterogeneity of cohesive granular matter, we conducted a torsional shear experiment under constant normal load (cf. Section 2.2). As the ratio of cohesion force to normal stress is $\eta = F_c/(\sigma x_{50,3}^2) \approx$

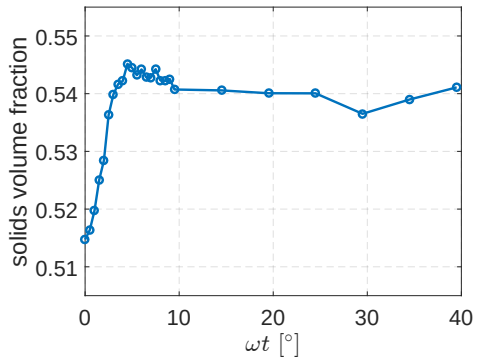

Figure 5: Global solids volume fraction in the shear cell over time, i.e., total particle volume divided by the volume enclosed between upper and lower piston.

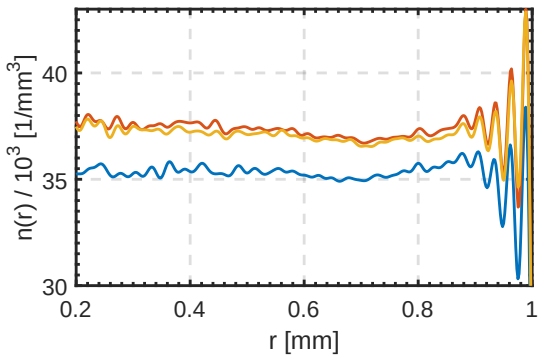

Figure 6: Radial density profiles (w = 8.8 µm) of the initial configuration (ωt = 0°), a compacted configuration (ωt = 4°) and a configuration towards the end of the experiment (ωt = 34.5°). The values are averaged over the region between upper and lower piston in vertical direction.

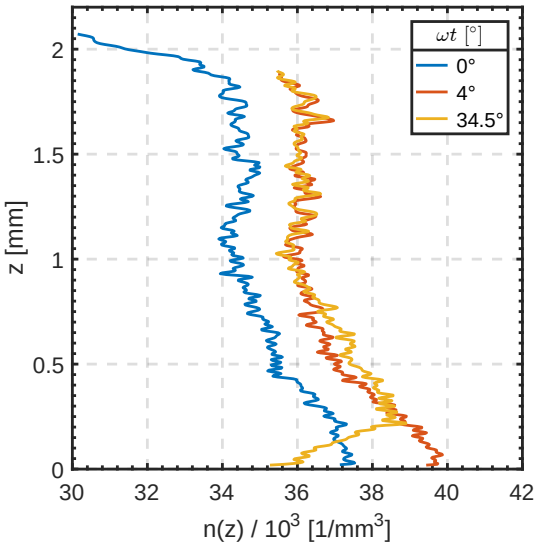

Figure 7: Axial density profiles (w = 8.8 µm) of the same configurations as used for the radial profiles (Figure 6). Due to densification and dilation, the height of the sample changes over time. In all plots z = 0 marks the upper edge of the vanes on the bottom piston.

0.2, only a minor influence of cohesion is expected [20]. The following analysis serves to demonstrate the capability of our methods in general and provides insights into structural heterogeneity as well as shear band formation and evolution in cohesive granular matter. Starting from a consolidated configuration, a total shear strain of $\omega t \approx 39.5°$ is analyzed. To describe the distribution of the powder within the shear cell, we analyze the spatially-resolved number density of particle centers (cf. Section 3.1). In the following, we present different methods to identify the shear band, based on tomographic images and particle tracking, respectively. The findings are presented in Sections 3.2 and 3.3 and allow for detailed characterization of shear band shape and location over time.

3.1. Segmentation and structural analysis

To extract particle positions from the experimental configuration, tomographic data was segmented as explained in Section 2.3.2. Particle positions and radii have been determined by calculating the center of mass and the volume-equivalent radius (i.e., the radius of a ball with the same volume) of the voxel representation of each particle. Particles with a diameter smaller than 13.2 µm or larger than 53.0 µm have been excluded from the analysis. Very small particles cannot be segmented reliably, while unrealistically large particles may occur due to bright, star-like artifacts, which seem to be caused by single particles of a different material present in the sample. Note that the excluded particles correspond to less than 0.1 % of the whole particle volume at each point in time.

The distribution of particle diameters extracted from the segmented image data is unimodal and slightly skewed to the left with a median of $x_{50,3}$ = 30.7 µm and an interquartile distance of $x_{75,3} - x_{25,3}$ = 3.7 µm. The size distribution has also been measured using laser diffraction (cf. Section 2.1), where a very similar median of $x_{50,3}$ = 29.8 µm was observed. The interquartile distance obtained from laser diffraction is $x_{75,3} - x_{25,3}$ = 11.0 µm, i.e., considerably larger than the value based on the image data. This is most likely due to the back calculation algorithm used for laser diffraction measurements, which is known to overestimate the width of extremely narrow particle size distributions [32]. Importantly, the particle size distribution estimated based on the image data is almost identical for all XMT measurements, indicating consistent segmentation results.

By estimating the total particle volume based on the binary images and normalizing with the volume of the sample chamber, we can track the global solids volume fraction over time, shown in Figure 5. An initial densification occurs up to $\omega t \approx 4°$ and is followed by a dilation until a steady state volume fraction is reached at a shear strain of $\omega t \approx 10°$. We notice, however, that the fluctuations in the experimental data do not support a final statement on when exactly the steady state is reached. The analysis of shear localization will lead to further insight (cf. Section 3.3).

Based on the centers of the segmented particles, we compare the number density $n(r, z)$, i.e., the number of particles per cubic millimeter, as a function of height (z) and distance to the central axis of the cylindrical sample chamber (r). The results are shown in Figures 6-8. Rotational invariance is assumed,

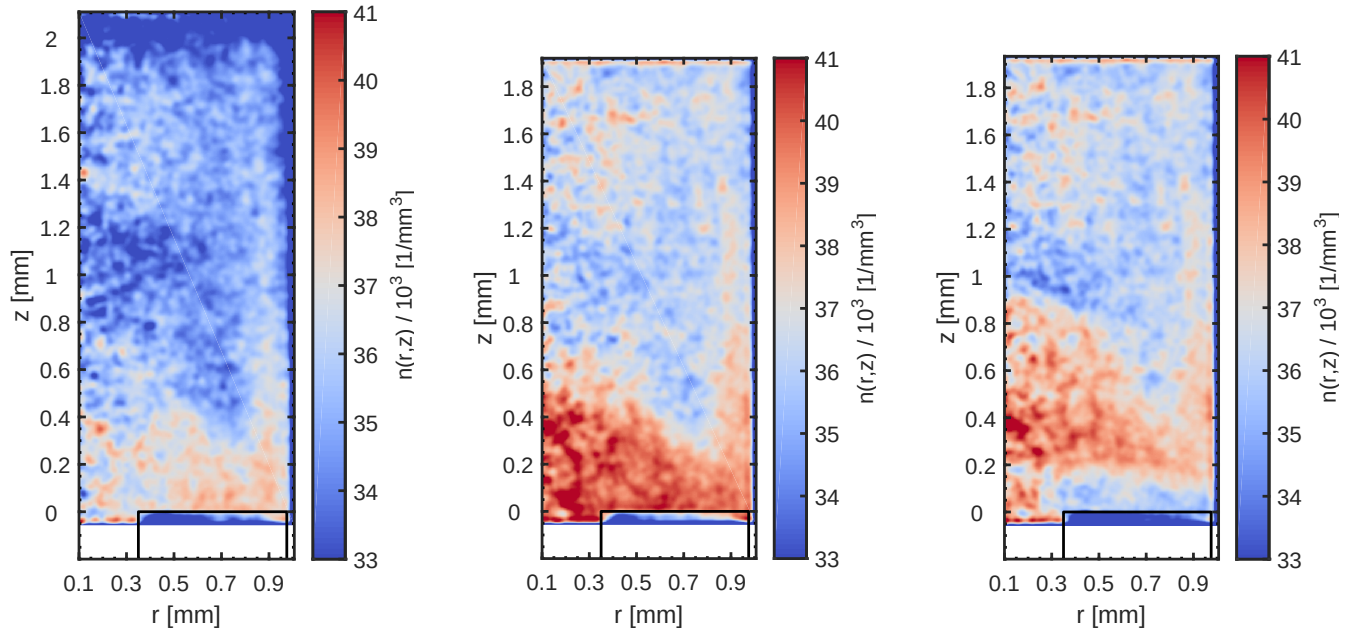

Figure 8: 2D density profiles (w = 14.9 µm) of the initial configuration (ωt = 0°; left), a compacted configuration (ωt = 4°; center) and a configuration towards the end of the experiment (ωt = 34.5°; right). The black frame in the bottom right corner marks the location of the vanes on the lower piston.

hence all data is averaged over φ. To obtain continuous fields, we coarse-grain the data with a Gaussian kernel (with standard deviation w).

Figure 6 shows radial number density profiles of the initial configuration, a compacted configuration and a configuration towards the end of the experiment, using a coarse-graining length of w = 8.8 µm. The radial density profiles reveal wall-induced layering, noticeable for all depicted configurations ($r > 0.9$ mm). This obvious signature of granular microstructure is known from shear experiments [9]. Moreover, all radial density profiles show the lowest number density at $r \approx 0.7$ mm. It increases very slightly towards the center of the shear cell and shows a more pronounced increase close to the wall. Judging by the radial density profiles, shearing leads to compaction.

This misconception can be cleared up by the axial density distribution, which is shown in Figure 7 for the same configurations. Displayed is the range between upper and lower piston, where $z = 0$ marks the upper edge of the lower piston. Comparing the configurations at the beginning and end of the experiment, a dilation ($0 \leq z \leq 0.2$ mm) as well as a densification zone ($z > 0.2$ mm) can be identified. Taking into account the intermediate profile, it can be observed that the densification is strongest and almost homogeneous before $\omega t = 4°$. Afterwards, the sample is only slightly further compressed between 0.3 mm $\leq z \leq$ 0.8 mm, which is a direct consequence of the strong dilation in the lower part of the shear cell. The dilation suggests a shear localization close to the lower piston, which will be analyzed in more detail in Sections 3.2 and 3.3.

The 2D number density plots (Figure 8) emphasize the spatial inhomogeneity of the density distribution, which was already revealed by the 1D profiles. As seen before, from bottom to top, a dilation zone is located directly above the lower piston, followed by a more densely packed zone, above which a homogeneous zone is located. A higher number density close to the wall can be observed as well. Ignoring the inhomogeneity induced by the capillary wall, the 2D density plots suggest a cone like densification zone on top of the lower piston. This unexpected feature can already be spotted in the initial configuration and may therefore be a relict of the preparation procedure, as discussed later (Section 4.1).

3.2. *Image-based local shear deformation*

The image-based local shear deformation was determined in 1D and 2D as described in Section 2.3.1, based on the tomographic grayscale image stacks. Results for the final four time steps are shown in Figure 9. We obtain an angle of local deformation as a function of the height in the sample (z) in 1D, and as a function of the height (z) *and* the distance from the central axis of the cylinder (r) in 2D. Note that based on the image data we only obtain a coarse radial resolution: The number of radial coordinates for which the local shear deformation is evaluated corresponds to the number of rings rotated independently (cf. Section 2.3.1). This number cannot be very large, because we need a certain number of voxels on each ring in order to get reliable results.

Shear strain localizes close to the lower piston, as already suggested by the density profiles. The 1D deformation (Figure 9, top) shows that the extension of the shear band still varies after $\omega t \approx 10°$, although the volume fraction already remains constant after this point (see Figure 5). Starting at $\omega t \approx 25°$ no significant changes in the deformation behavior can be observed. In the 2D deformation (Figure 9, bottom) we obtain more details about the geometric shape of the shear band. In

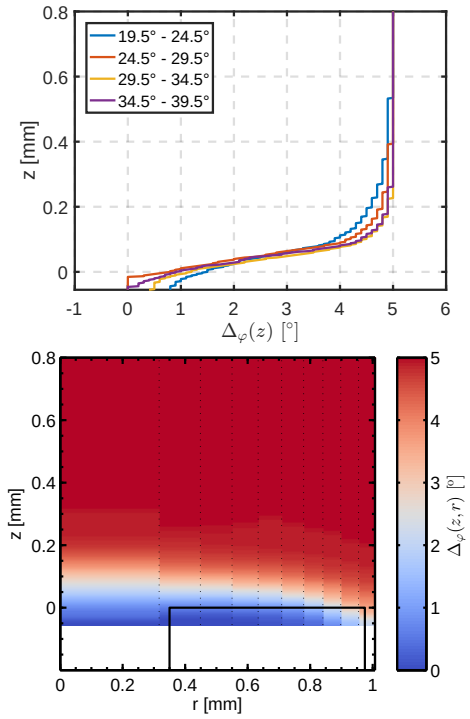

Figure 9: Image-based local shear deformation in 1D and 2D in the steady state of the experiment. The 1D case (top) shows the shear deformation as a function of the height in the sample with almost congruent states. The 2D deformation, which is shown for the last time step as an example (bottom), reveals that the shear band geometry is curved close to the wall.

addition to its location and width, the 2D deformation reveals that the shear band is curved downwards where the vanes on the lower piston meet the cylinder wall. This means that directly above the lower piston particles close to the wall have a higher angular velocity than particles in the center of the sample. Again, the effect can be explained by the influence of the outer rotating wall because outer particles are more easily dragged along than particles in the center of the sample. We observe a vertical extension of the shear band of up to 250 µm after $\omega t \approx 25°$, which corresponds to approximately 8 median particle diameters. This agrees well with data from literature, where ratios between 7 and 18 have been found [11, 14, 28, 33]. The 2D deformation additionally suggests that the shear band is broader towards the center of the sample than close to the outer wall.

The 1D image-based local shear deformation can also be used to measure the rotation of the upper and lower piston (see Section 2.3.1). In principle, the movement of the pistons should be known from the setup of the experiment: the upper piston should rotate in steps of 0.5° and later 5°, while the lower piston should be held perfectly still. However, we observe that the actual movement of the pistons deviates from this ideal. The mean absolute difference between the actual and target angle of rotation is 0.02° for the upper and 0.19° for the lower piston, respectively. Taking into account both, the mean absolute difference between the actual and target angle of shear is 0.20°.

This imperfection in the rotational movement is likely caused by the compensation unit, which is supposed to keep the contactless mounted lower piston in place while tracking shear stress. However, interlocking of particles between piston and wall may counteract this mechanism, dragging the lower piston partially during shear deformation and resulting in implausible high peaks in the shear stress. A solution for this problem can be obtained by decreasing the piston diameter (and thus increasing the gap) to reduce the effects of interlocking. However, this is accompanied by the more disadvantageous effect of loosing sample material, which may be pushed through the gap and out of the sample chamber during shear. Moreover, we can only control the rotation of the upper piston and hence of the glass capillary in this shear-tester setup. Unfortunately, it is not possible to observe the rotation of the lower piston in the range of $\approx 0.01°$ during shear deformation to achieve the desired relative rotation.

3.3. Tracking and shear bands

Particle tracking allows for an even more detailed analysis of strain localization in the experiment compared to the image-based analysis of Section 3.2.

Particle tracks were computed for all steps of shearing starting at $\omega t = 3.5°$ using the methods described in Section 2.3.3. Before this point we observe a considerable decrease in the distance between upper and lower piston, from 2.12 mm to 1.93 mm, which leads to considerably high vertical displacements of particles in the upper part of the cylinder. This shear-induced densification, which is even spatially inhomogeneous, renders the identification of reliable tracks in the first time steps impossible. After $\omega t = 3.5°$ we obtained very good tracking results. The tracking efficiency (measured as the number of particles assigned to valid tracks divided by the total number of particles) is larger than 97 % in each step of 5°, and even larger than 99.5 % in each step with an angle increment of 0.5°.

On the basis of particle tracks, it is possible to calculate velocities of single particles in the experiment. For reasons of comparability, all particle velocities are described as angular velocities with respect to the axis of rotation (cf. Section 2.3.4), and normalized to the interval $[0, 1]$ using the movements of upper and lower piston, which are estimated as described in Section 2.3.1.

We computed 2D profiles of average normalized angular velocity, $v_{\tilde{\varphi}}(\tilde{r}, z)$, as a function of height (z) and (horizontal) distance to the axis of rotation ($\tilde{r}$), where the average is in $\tilde{\varphi}$-direction and $(\tilde{r}, \tilde{\varphi}, z)$ denote cylindrical coordinates with respect to the axis of rotation. A (time-averaged) example is shown in Figure 10 on the right-hand side. Note that the axis of rotation has been estimated from the data as described in Section 2.3.4 and rotational velocities are calculated with respect to this estimated axis. This change of the coordinate system is necessary because the dynamics in the sample clearly depend on the distance from the axis of rotation rather than the distance from the central axis of the cylinder. Without adjusting the cylindrical coordinates, the experimental particle velocities would not be independent of φ and averaging in azimuthal direction would not be feasible. For coarse-graining we chose the

same bandwidth as for the 2D density profiles in Section 3.1, $w = 14.9$ µm.

In order to describe the shear bands quantitatively, we fitted a parametric function to the velocity profiles. For a fixed radial distance, $\tilde{r}$, the velocity profile is described well by the function

$$v_{\tilde{\varphi}}(z) = \frac{1}{2} + \frac{1}{2}\ \mathrm{erf}\left(\frac{z - z_{sb}}{w_{sb}}\right), \tag{5}$$

where erf denotes the error function, and z_{sb} and w_{sb} are the fitted parameters describing the local height and (semi) width of the shear band, respectively. This function is attractive because of its simplicity with only two parameters and has also been used in [10] to describe symmetric shear zones. Discretizing $\tilde{r}$ with a bin size of 0.03 mm and fitting this function to the z-coordinates and (normalized) velocities of the particles in each bin, we obtain estimates of $z_{sb} = z_{sb}(\tilde{r})$ and $w_{sb} = w_{sb}(\tilde{r})$ as functions of the radial distance $\tilde{r}$, leading to a $\tilde{r}$-dependent velocity profile, $v_{\tilde{\varphi}}(z) = v_{\tilde{\varphi}}(\tilde{r}, z)$. Here, we define the shear band as the interval $z_{sb} \pm w_{sb}$, which covers approximately the central 84 % of the velocity range in the data. Of course, any other reasonably large percentage could be chosen to separate shear band and homogeneous zones in principle. Since the main purpose of the fit is to quantitatively compare the experimental shear band width and location between different points in time, we stick to this simple choice.

An example of actual and fitted velocity profiles as well as the time-averaged velocity profile obtained for the data after $\omega t = 10°$ is reached are shown in Figure 10. The fitted shear band is indicated as $z_{sb} \pm w_{sb}$ in the graph on the right-hand side. Both graphs show a very good agreement of the fitted profiles with experimental data. The 2D profile shows that the shear band is close to the lower piston, on average (over $\tilde{r}$) its center is at a height of $z = 0.12$ mm. The shear band has a width of $2w_{sb} = 0.23$ mm on average, which corresponds to roughly 8 median particle diameters. It is slightly curved downwards where it comes close to the outer wall of the cylinder.

Figure 11 shows the development of z_{sb} and w_{sb} over time, averaged over $\tilde{r}$. It seems that a steady state is reached at $\omega t \approx 10°$, as already indicated by the solids volume fraction shown in Figure 5. Before $\omega t \approx 10°$ the shear band width and height are (on average) larger, and both values fluctuate much more strongly. The shear band rises from $z_{sb} \approx 0.15$ mm to $z_{sb} \approx 0.37$ mm in this period and drops back to its lower position at a shear strain of $\omega t \approx 9°$. However, even after $\omega t \approx 10°$ the shear band width fluctuates perceptibly, w_{sb} takes values between 0.08 and 0.16 mm here. Smaller fluctuations have to be expected since we consider (and implicitly average over) much larger time intervals in each step here. There seems to be a second drop in the variability of z_{sb} and w_{sb} at $\omega t \approx 25°$. Whether this is a coincidence or the steady state is actually only reached in the last three steps of the experiment is unclear and cannot be judged based on the present data. Therefore, we assume that the steady state is reached at $\omega t \approx 10°$ in our analysis.

4. Discussion

The analysis in Section 3 demonstrated that our methods allow to extract valuable information on particle dynamics in space and time. In the following, we discuss several interesting effects revealed by the analysis and compare the presented methods for shear band analysis in terms of computational cost and level of detail.

4.1. Segmentation and structural analysis

Analysis of the static configurations revealed an inhomogeneous packing density within the sample (cf. Figures 6-8). The axial number density profiles show a prominent gradient in z-direction in the lower part of the shear cell, which is caused by wall friction and demonstrates the stress-flux between piston and capillary. At the beginning of the experiment, the number density directly below the upper piston is much lower than in the rest of the shear cell (cf. Figures 7 and 8). This happens most likely because particles do not fill the top part of the shear cell uniformly after they are sieved into the sample chamber. Apparently, uniaxial compression (as applied prior to shearing) is not sufficient to spread these particles out evenly. The number density in this region normalizes only after shearing has started ($\omega t = 4°$).

In addition, the 2D number density profiles (Figure 8) show that an almost cone-shaped densification zone is present in the center of the shear cell. This seems puzzling at first, but may also originate from the preparation procedure. As described in Section 2.2.2, the preparation process is a gravitation driven deposition. The first portion of dumped particles piles onto the structured bottom piston (e.g. vanes arranged in a star shape), which quite likely dictates the densification zone's shape. Of course this interpretation needs further investigation.

4.2. Tracking and shear bands

In Sections 3.2 and 3.3 we presented the results of different methods to analyze shear bands in the experiment. Though they are in good agreement in principle, the methods vary in computational efficiency, flexibility and the level of detail of the information they provide. The 1D image-based local shear deformation is relatively fast to compute and provides a good first overview over the deformation as a function of the height in the sample. An extension of this method is the 2D image-based local shear deformation. Here, each image slice is not rotated as a whole — instead, the disk-shaped cross section of the cylinder is subdivided into disjoint rings, which are rotated independently (see Section 2.3.1). This extension is more computationally expensive (depending on the number of rings used), but in return provides 2D information: the local angle of shear deformation as a function of height *and* radial coordinate in the sample. In particular, it reveals that the shear band in our data is slightly curved and not exactly parallel to the xy-plane (cf. Figure 9, bottom). We believe that the curved shape of the shear band is predominantly provoked by the influence of the outer glass wall. Such effects are concealed by the 1D deformation, which is similar to an average over r. If the shear band properties depend strongly on the radial coordinate,

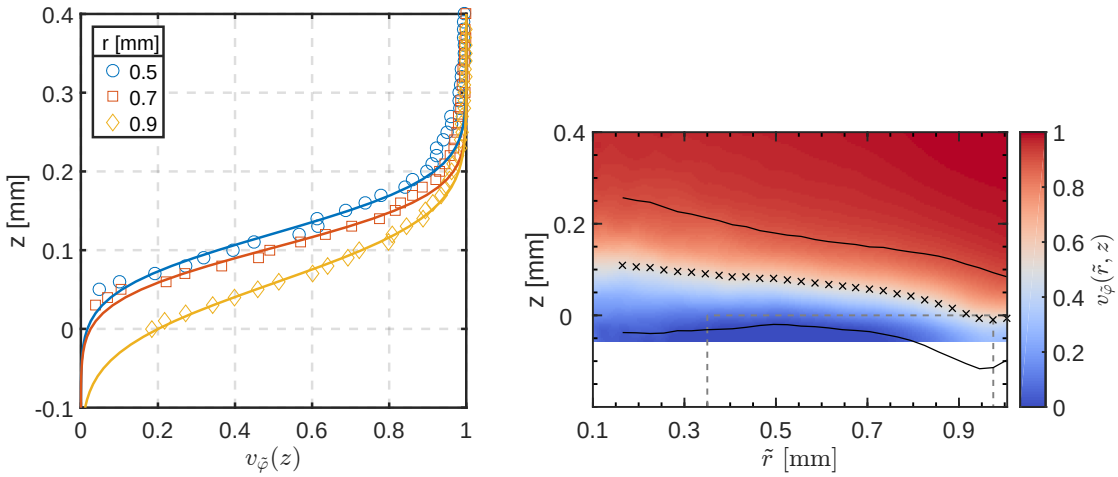

Figure 10: Example of actual and fitted velocity profiles for one time step (29.5° - 34.5° of shearing) and different distances from the axis of rotation (left), and 2D velocity profile after $\omega t = 10^{\circ}$ with the fitted shear band indicated in black as $z_{sb} \pm w_{sb}$ (right).

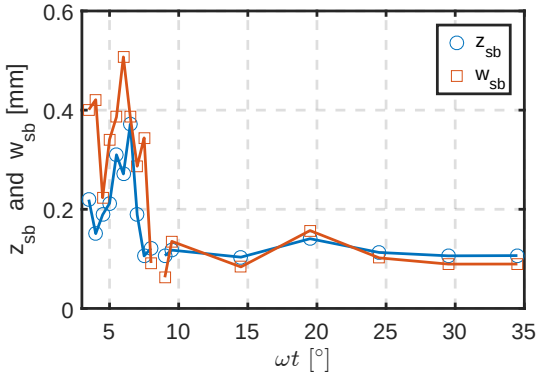

Figure 11: Development of the fitted shear band width and location over time, averaged over $\tilde{r}$.

the 1D information might even be misleading. For example, a shear band which is actually narrow and strongly curved (which might, e.g., be caused by a strong sample heterogeneity) would seem like a wide shear band in the 1D deformation. In our case the shear band is only slightly curved and we obtain similar shear band widths with both methods. On that account the observed shear band width in our experiment agrees well with data in literature for noncohesive granular matter. With the ratio $F_c/(\sigma x_{50,3}^2) \approx 0.2$, this is expected [34].

The results presented in Section 3.3 were computed based on a particle tracking. Obtaining this particle tracking requires significant additional effort during the experiment as well as from a computational and analytic perspective. First, the XMT measurements are time consuming and a sufficient temporal resolution is needed. Although we present a method to track the particles even in steps with an angle increment of 5°, much smaller angle increments are needed at least for part of the experiment to validate the method (see Section 2.3.3). Furthermore, the tracking itself requires a preceding segmentation of high quality and the 2D image-based local shear deformation discussed in the previous paragraph. In return, it provides unique and valuable information on the motion of single particles based on experimental data, which allows for a most accurate shear band analysis (cf. Figures 10 and 11). It is much more precise than purely image-based methods and revealed, for example, variations of the axis of rotation (cf. Figure 4). Effects like this cannot be captured and accounted for by the image-based local shear deformation. Moreover, particle tracking bridges the gap between experimental data and discrete element simulations regarding particle motion behavior and hence, allows for a direct comparison of both worlds. It enables the estimation of continuous velocity fields and a parametric fit of the shear band parameters in very fine radial resolution. Though not performed in this study, the particle tracking additionally allows for the comparison of single particle trajectories and their properties, which will be subject of future work.

The Gaussian function given in Equation (5), which we used for fitting the shear bands, proved to provide very good fits for shear bands in a modified Couette shear cell [10]. These shear bands develop distant from a wall, resulting in a symmetric shape. When shear bands develop close to a wall, such perfectly symmetric shapes are not typical. For example, a mixture of a Gaussian and an exponential component in the velocity profile was observed in a study of shear bands localized close to the side wall in a similar shear cell geometry [8, 9]. The exponential decay was attributed to slippage between layers of the monodisperse particles used in [9]. In our data the velocity profiles appeared approximately symmetric, thus we consider only the purely Gaussian fitting function. If an exponential component is present in our data, it is very small. This is plausible because we cannot have layers of particles at the bottom of the cylinder due to the structured pistons. A wider particle size distribution might be another reason why we do not observe layers of particles slipping over each other at the bottom of the shear cell in this study.

5. Conclusions and outlook

In this study we demonstrated that a torsional shear experiment can be realized on a very small scale. We used spherical

particles made of borosilicate glass. The combination of micro shear-tester and XMT allows to capture the evolution of the sample in a series of high-resolution 3D images. In addition, we presented a toolbox of methods to analyze a shear experiment based on time-resolved tomographic image data. Particle positions and radii could be extracted consistently from the image data and have been used to compute spatially resolved number density profiles of the particle centers, revealing structural inhomogeneities. Furthermore, we presented methods to assess the local shear deformation based on image data. We demonstrated how this information can be used to identify tracks of single particles even when a large angle increment of up to 5° is used for shearing between XMT measurements. Our analysis showed that the shear band developed close to the lower piston and was slightly curved downwards at the outer wall of the cylinder. Using a Gaussian function to fit profiles of rotational velocities, we could quantitatively describe the development of shear band width and location in time and space.

The main benefit of this study is that it paves the way for a direct comparison of experiments and DEM simulations, and hence, provides an improved basis for the calibration and validation of numerical models. A next step for future research is to simulate the same experiment and to use the data provided by our methods for a comparison of both approaches. On the experimental side, an extension of the parameters measured during shear is possible. Here, a shear stress logging during deformation and an investigation of the effect of larger stress levels on the packing and deformation behavior is desirable. Another raising question, which cannot be answered in detail by the current study, is how the sample preparation process affects the initial packing behavior. Finally, additional scenarios with varied particle properties should be addressed to describe their effect on the structure and dynamics of fine granular matter experimentally. Possible variations include nonspherical particle shapes (e.g. rods and irregular shapes), particle surface modifications (e.g. to vary cohesion forces) and broader or multimodal particle size distributions. For nonspherical particles, it would additionally be possible to follow the rotation of individual particles.

Acknowledgments

We kindly thank Alexander Weuster, Dietrich Wolf and Lothar Brendel from the University of Duisburg-Essen for their valuable contributions to discussions and for their detailed comments on this manuscript. This work was funded and prepared within the priority program SPP 1486 by the Deutsche Forschungsgemeinschaft (DFG).

References

[1] M. A. Polizzi, J. Franchville, J. L. Hilden, Assessment and predictive modeling of pharmaceutical powder flow behavior in small-scale hoppers, Powder Technol. 294 (2016) 30–42.

[2] Y. Tian, P. Lin, S. Zhang, C. Wang, J. Wan, L. Yang, Study on free fall surfaces in three-dimensional hopper flows, Adv. Powder Technol. 26 (2015) 1191–1199.

[3] M. C. Garcia, H. J. Feise, S. Strege, A. Kwade, Segregation in heaps and silos: Comparison between experiment, simulation and continuum model, Powder Technol. 293 (2016) 26–36.

[4] K. Grudzien, M. Niedostatkiewicz, J. Adrien, E. Maire, L. Babout, Analysis of the bulk solid flow during gravitational silo emptying using X-ray and ECT tomography, Powder Technol. 224 (2012) 196–208.

[5] H. M. Jaeger, S. R. Nagel, Physics of the granular state, Science 255 (1992) 1523–1531.

[6] F. Da Cruz, S. Emam, M. Prochnow, J.-N. Roux, F. Chevoir, Rheophysics of dense granular materials: discrete simulation of plane shear flows, Phys. Rev. E 72 (2005) 021309.

[7] K. Kamrin, G. Koval, Nonlocal constitutive relation for steady granular flow, Phys. Rev. Lett. 108 (2012) 178301.

[8] A. Ries, L. Brendel, D. E. Wolf, Shearrate diffusion and constitutive relations during transients in simple shear, Comput. Part. Mech. 3 (2016) 303–310.

[9] D. M. Mueth, G. F. Debregeas, G. S. Karczmar, P. J. Eng, S. R. Nagel, H. M. Jaeger, Signatures of granular microstructure in dense shear flows, Nature 406 (2000) 385–389.

[10] D. Fenistein, J. W. van de Meent, M. van Hecke, Universal and wide shear zones in granular bulk flow, Phys. Rev. Lett. 92 (2004) 094301.

[11] S. Nemat-Nasser, N. Okada, Radiographic and microscopic observation of shear bands in granular materials, Géotechnique 51 (2001) 753–765.

[12] R. Moosavi, M. R. Shaebani, M. Maleki, J. Török, D. E. Wolf, W. Losert, Coexistence and transition between shear zones in slow granular flows, Phys. Rev. Lett. 111 (2013) 148301.

[13] F. Varnik, L. Bocquet, J.-L. Barrat, L. Berthier, Shear localization in a model glass, Phys. Rev. Lett. 90 (2003) 095702.

[14] C. M. Gourlay, A. K. Dahle, Dilatant shear bands in solidifying metals, Nature 445 (2007) 70–73.

[15] R. Fuchs, T. Weinhart, J. Meyer, H. Zhuang, T. Staedler, X. Jiang, S. Luding, Rolling, sliding and torsion of micron-sized silica particles: experimental, numerical and theoretical analysis, Granul. Matter 16 (2014) 281–297.

[16] S. Strege, A. Weuster, H. Zetzener, L. Brendel, A. Kwade, D. E. Wolf, Approach to structural anisotropy in compacted cohesive powder, Granul. Matter 16 (2014) 401–409.

[17] I. Vlahinić, E. Andò, G. Viggiani, J. E. Andrade, Towards a more accurate characterization of granular media: Extracting quantitative descriptors from tomographic images, Granul. Matter 16 (2013) 9–21.

[18] C. Thornton, L. Zhang, On the evolution of stress and microstructure during general 3D deviatoric straining of granular media, Géotechnique 60 (2010) 333–341.

[19] F. A. Gilabert, J.-N. Roux, A. Castellanos, Computer simulation of model cohesive powders: plastic consolidation, structural changes, and elasticity under isotropic loads, Phys. Rev. E 78 (2008) 031305.

[20] P. G. Rognon, J.-N. Roux, M. Naaim, F. Chevoir, Dense flows of cohesive granular materials, J. Fluid Mech. 596 (2008) 21–47.

[21] P. W. Cleary, Industrial particle flow modelling using discrete element method, Eng. Comput. 26 (2009) 698–743.

[22] M. Raffel, C. E. Willert, S. Wereley, J. Kompenhans, Particle Image Velocimetry: A Practical Guide, Springer, Heidelberg, 2013.

[23] M. Ostendorf, J. Schwedes, Application of particle image velocimetry for velocity measurements during silo discharge, Powder Technol. 158 (2005) 69 – 75.

[24] J. Choi, A. Kudrolli, M. Z. Bazant, Velocity profile of granular flows inside silos and hoppers, J. Phys.: Condens. Matter 17 (2005) S2533.

[25] C. Cierpka, B. Lütke, C. J. Kähler, Higher order multi-frame particle tracking velocimetry, Exp. Fluids 54 (2013) 1533.

[26] H. G. Maas, A. Gruen, D. Papantoniou, Particle tracking velocimetry in three-dimensional flows, Exp. Fluids 15 (1993) 133–146.

[27] J. Wenzl, R. Seto, M. Roth, H.-J. Butt, G. K. Auernhammer, Measurement of rotation of individual spherical particles in cohesive granulates, Granul. Matter 15 (2013) 391–400.

[28] S. Strege, Röntgenmikrotomographische Analyse der Verdichtung und Scherung feiner und kohäsiver Pulver, Ph.D. thesis, TU Braunschweig (2014), ISBN: 978-3868446647.

[29] E. R. Doughtery (Ed.), Mathematical Morphology in Image Processing, Marcel Dekker Inc., New York, 1993.

[30] T. W. Ridler, C. S, Picture thresholding using an iterative selection method, IEEE T. Syst. Man Cyb. 8 (1978) 630–632.

[31] J. C. Crocker, D. G. Grier, Methods of digital video microscopy for colloidal studies, J. Colloid Interf. Sci. 179 (1996) 298–310.
[32] R. Xu, Particle Characterization: Light Scattering Methods, Kluwer Academic Publishers, New York, 2002.
[33] P. Guo, Critical length of force chains and shear band thickness in dense granular materials, Acta Geotech. 7 (2012) 41–55.
[34] A. Singh, V. Magnanimo, K. Saitoh, S. Luding, Effect of cohesion on shear banding in quasistatic granular materials, Phys. Rev. E 90 (2014) 022202.